



Dynamic development of geochemical reaction fronts during hydraulic stimulation of shale

Vincent Noël^{a,b,*}, Jennifer L. Druhan^{b,c}, Asli Gundogar^{d,1}, Anthony R. Kavscek^b, Gordon E. Brown Jr.^{a,b,e}, John R. Bargar^{a,b}

^a Stanford Synchrotron Radiation Lightsources, SLAC National Accelerator Laboratory, 2575 Sand Hill Road, Menlo Park, CA, 94025, USA

^b Center for Mechanistic Control of Unconventional Formations (CMC-UF), Stanford University, Stanford, CA, 94305-2115, USA

^c Department of Geology, University of Illinois, 1301 W Green St., Urbana, IL, 61801, USA

^d Department of Energy Resources Engineering, School of Earth, Energy & Environmental Sciences, Stanford University, Stanford, CA, 94305, USA

^e Department of Geological Sciences, School of Earth, Energy & Environmental Sciences, Stanford University, Stanford, CA, 94305-2115, USA

ARTICLE INFO

Keywords:

Geochemical reaction front
Mineral dissolution
Matrix alteration
Reactive transport
Hydraulic stimulation
Unconventional shale
Synchrotron-based X-ray fluorescence microprobe

ABSTRACT

Injection of acidic hydraulic fracture fluid (HFF) into shale formations for unconventional oil/gas production results in chemical reactions in the shale matrix that can alter fluid transport. Here, we report the results of set of experiments designed to evaluate the impact of calcite dissolution as a function of carbonate mineral content on matrix chemical reactivity and pore-space modification concomitant with imbibition. We tracked acidic HFF transport in four samples of Wolfcamp shale with calcite contents varying from 4% to 59% by monitoring the rate and spatial extent of bromide tracer transport using synchrotron-based X-ray fluorescence microprobe (XFM) imaging. Concurrently, we also carried out XFM imaging of the spatial distribution of Ca in the Wolfcamp shale cores (as a proxy of calcite distribution). Our approach thus yields a direct record of time-resolved selective ion transport resulting from the penetration of acidic HFF and the associated mineral transformations in the shale cores.

We show that the variability in calcite content of Wolfcamp shale samples can directly affect the rate and spatial extent of imbibition. Although reaction of the acidic HFF with carbonates in shales enhances calcite dissolution and increases porosity, the spatial extent of calcite dissolution in the shale matrix is limited due to a rapid neutralization of pH. The relative abundance and spatial distribution of calcite control the chemical saturation state of the HFF progressing into the matrix. As a result, calcite has a major impact on the spatial extent and rate of matrix alteration and thus on HFF transport during subsurface reservoir stimulation. Consequently, increased calcite content in the shale matrix inhibits the spatial extent of the pore-volume increase and, by extension, the spatial extent and rate of imbibition.

Our results thus show that the overall rates of calcite dissolution approach the rates of acidic HFF transport (*i.e.*, Damköhler number ~ 1), which could contribute to the efficiency of subsurface reservoir stimulation. A better understanding of HFF-calcite reaction rates is crucial for improving the prediction and optimization of fluid transport across HFF-shale interfaces during hydraulic fracturing.

1. Introduction

Deep subsurface energy systems rely upon controlled fracture stimulation of the host rock using hydraulic fracture fluid (HFF) to enable

production of heat (Li and Horne, 2010; Ganguly and Kumar, 2014) and hydrocarbons (Ma et al., 1997; Zhou et al., 2000; Abd et al., 2019) and to enhance oil/gas recovery while storing CO₂ (Krevor et al., 2012; El-Maghraby and Blunt, 2013; Tokunaga et al., 2013). Concentrated

Abbreviations: Br, Bromide; XFM, X-ray Fluorescence Microprobe; CT, Computed Tomography; XRF, X-ray Fluorescence; NETL, National Energy Technology Laboratory; HFF, Hydraulic Fracturing Fluid; SSRL, Stanford Synchrotron Radiation Lightsources; TST, Transition State Theory; SEM, Scanning Electron Microscopy; DOE, Department of Energy; CMC-UF, Center for Mechanistic Control of Water-Hydrocarbon-Rock Interactions in Unconventional and Tight Oil Formations.

* Corresponding author. Stanford Synchrotron Radiation Lightsources, SLAC National Accelerator Laboratory, 2575 Sand Hill Road, Menlo Park, CA, 94025, USA.

E-mail address: noel@slac.stanford.edu (V. Noël).

¹ Currently, at the Department of Energy Systems Engineering, Izmir Institute of Technology, 35430, Urla, Izmir, Turkey

<https://doi.org/10.1016/j.apgeochem.2022.105542>

Received 4 May 2022; Received in revised form 28 November 2022; Accepted 4 December 2022

Available online 6 December 2022

0883-2927/© 2022 Elsevier Ltd. All rights reserved.

hydrochloric acid (HCl) solutions are among the most common additives in water-based HFF used to initiate hydraulic fracturing in unconventional shale reservoirs (Stringfellow et al., 2014). Such additives create strong disequilibrium conditions in oil/gas shales (Haluszczak et al., 2013; Orem et al., 2014; Lester et al., 2015; Rowan et al., 2015; Shih et al., 2015; Ziemkiewicz and He, 2015; Renock et al., 2016; Zolfaghari et al., 2016; Harrison et al., 2017) and initiate imbibition of acidic HFF into the shale matrix as well as myriad chemical reactions that lead to dissolution of acid-sensitive minerals such as calcite (Harrison et al., 2017). They also promote the development of chemical alteration fronts that propagate into the matrix interior (Li et al., 2019a, 2020). Concurrently, dissolution of calcite consumes acidity, causing an increase in pH and precipitation of secondary (scale) minerals.

While the basic geochemical trajectory of HFF-fracture face interactions is understood, the dynamics and details of these complex, rapidly evolving geochemical systems remain largely uncharacterized at the spatial scale of reaction fronts (i.e., 10^{-7} to 10^{-4} m), where transport and reaction are strongly coupled (Li et al., 2020). HFF-shale interfaces are expected to be complex due to the potential for feedback between rapid transport (imbibition) and rapid matrix alteration (dissolution). Moreover, given that the imbibition process is strongly dependent on the porosity and permeability of the porous media (Rangel-German and Kovesek, 2002; Tokunaga, 2020), such coupling is expected to impact the rate and spatial extent of HFF penetration into the shale interior, and ultimately the capacity of HFF to enhance communication between fractures and the surrounding reservoir. More specifically, if the overall rates of calcite dissolution approach the rates of HFF transport (i.e., Damköhler number ~ 1), then accessible porosity and pH of acidic HFF should increase within the reaction front on a timescale similar to that of HFF imbibition. Under these conditions, well-defined reaction fronts can develop (0–200 μm thick from HFF-shale interface; Li et al., 2019a). If HFF imbibition is fast compared to calcite dissolution (i.e., Damköhler number $\ll 1$), then acid will initially imbibe into the matrix without being neutralized. Under these reaction rate-limited conditions, dissolution would occur over a relatively large area, causing the reaction front to be diffuse and porosity enhancement to be homogeneously distributed in the matrix. Overall, the extent of coupling between reaction and transport could strongly influence the distribution of secondary porosity, and thus, the transport and chemical properties of the interface. This relationship is worth considering for the improvement of simulation of flow and reactive transport processes (Evje and Hiorth, 2011; Hall, 2019; Cai et al., 2020).

The most rapid and ubiquitous reactive alteration process in the fractured shale systems is typically carbonate dissolution (e.g., calcite, dolomite; Jew et al., 2017; Harrison et al., 2017). It is therefore plausible that the acidity and chemical composition of HFF advancing into the reservoir, and the consequent increase in porosity, depend on the presence, availability, and dissolution rates, of the calcite. We, therefore, posit that the relative abundance and spatial distribution of calcite should be the master variables controlling matrix alteration.

In this study, we used synchrotron-based X-ray Fluorescence Microprobe (XFM) mapping to resolve simultaneously the extent of transport of acidic HFF into shale fracture faces, the enhancement of matrix porosity, and the products of chemical reactions in shale matrices across reaction fronts (micrometer to millimeter length scales). Wolfcamp cores with a wide range of calcite content (4%–59%) were selected to evaluate the role of carbonate as a master variable controlling shale matrix alteration. The rate and spatial extent of acidic HFF advancement in Wolfcamp shale cores was evaluated by mapping bromide (Br) tracer transport, whereas porosity enhancement was assessed by imaging the loss of Ca (i.e., dissolution of calcite). Matrix alteration was also tracked using synchrotron-based transmission μ -Computed Tomography (μ -CT) imaging and changes in solute concentrations in the surrounding fluid. Based on these measurements, we were able to show that HFF transport and the spatial distribution of reaction fronts do indeed vary with calcite abundance. We also showed that the enhancement of porosity following

the initial imbibition step is consistent with acid-driven opening of pore space that facilitates a secondary imbibition process. The results of this study support the development of new conceptual frameworks and numerical models of acidic HFF transport within shale reservoirs containing readily solubilized mineral phases such as carbonates.

2. Material and analytical procedures

2.1. Material and experimental details

2.1.1. Wolfcamp shale

Core samples for the Wolfcamp shale were obtained from the Hydraulic Fracturing Test Site #1 in Midland Basin, West Texas, and provided by the Gas Technology Institute (Gale et al., 2018). Four Wolfcamp shale samples were selected with different percentages of calcite and different depths (Table 1): 4% from 2910 m depth, 6% from 2890 m depth, 22% from 2888 m depth, and 59% from 3555 m depth. The mineralogical compositions of the Wolfcamp shale samples were determined by Fourier-transform infrared spectroscopy along a core of 10 cm length (see Table 1). The elemental compositions of the powdered Wolfcamp shales were determined by X-ray Fluorescence (XRF) spectrometry with a SPECTRO XEPOS energy dispersive XRF spectrometer equipped with a Pd cathode and operating at 50 kV and 40 mA at the Stanford Environmental Measurements Facility. The NIST 2711 certified reference material was intercalated in beginning and end of each analytical series. XRF measurements revealed that Br concentration in the selected Wolfcamp shale samples is $\leq 50 \mu\text{g/g}$.

From each selected Wolfcamp shale sample, a series of four adjacent 7 mm diameter and 1.2 cm height shale cores were drilled parallel to bedding to minimize sample heterogeneity. For each Wolfcamp shale sample, one shale core was immediately saved for each selected Wolfcamp shale samples and is consequently referred to as an 'initial' shale core. The density and porosity of the crushed 'initial' shale cores (i.e., before immersion of the shale in acidic HFF) were measured by helium pycnometry and mercury intrusion porosimetry. Grain volumes based on Boyle's Law were determined using a Micromeritics AccuPyc II 1340 helium pycnometer, and a Micromeritics AutoPore IV Series mercury porosimeter was used for bulk volume determination of the crushed and sieved (2–4 mm) samples. Using bulk volumes from mercury intrusion data, the helium porosities of the Wolfcamp samples range between 2 and 6% (Table 2).

2.1.2. Synthesis of acidic HFF

The acidic (pH = 1.4) HFF was synthesized based on the composition of the injection fluid used at the National Energy Technology Laboratory's (NETL) Marcellus Well E in Greene County, PA (Table SM-1; Hammack et al., 2014). The base fluid was made from Milli-Q water. Two modifications made to the HFF recipe were: (1) Omission of silica proppant, and (2) omission of two biocides that are at very low concentrations (2,2-dibromo-3-nitropropionamide and dibromoacetonitrile) compared to the added polyethylene glycol (Table SM-1). These exclusions are not expected to impact the HFF-shale interactions. NaBr solutions were systematically added to all laboratory-generated fluids (15 wt% HCl acid spearhead and HFF; see §2.1.3) to reach a concentration of 1 M NaBr in each solution. Br⁻ aqueous solute was used as an inert (low reactivity) tracer of the fluid penetration (Beulke et al., 2004; Ghane et al., 2019; Kastrinos et al., 2019). Goldberg and Kabengi (2010) demonstrated that Br⁻ sorption is mainly driven by a decrease in pH (pH < 7) and an increase in clay mineral content. In our experiments, the behavior of the accumulation of Br⁻ in the matrix was reversed. We show that with decreasing clay content and increasing pH, the accumulated mass of Br⁻ in the shale increased (Figure SM-1). We conclude that the accumulation of Br in the matrix in our experiments is not the consequence of Br⁻ sorption. Thus, we assume that Br⁻ is a good tracer for comparing acidic HFF penetration into shale samples with different calcite contents.

Table 1

Wolfcamp shale sample mineral composition before immersion in acidic HFF (= *initial state*) as determined by Fourier-transform infrared spectroscopy.

Sample ID	Depth (m)	Whole Rock Mineralogy (Weight %)								
		Quartz	K-Feldspar	Plagioclase	Chlorite	Illite-Smectite-Mica	Calcite	Ankerite-Dolomite	Pyrite	Organic Matter
4%-calcite	2910	43	2	6	1	35	4	4	3	2
6%-calcite	2890	41	3	8	1	31	6	3	4	3
22%-calcite	2888	32	2	6	2	22	22	11	3	1
59%-calcite	3555	20	1	2	0	7	59	8	1	0

Table 2

Bulk density, grain (matrix) density, and helium porosity of the crushed and sieved (2–4 mm) Wolfcamp shale samples before immersion in acidic HFF (= *initial state*).

Calcite amount	Grain Density (g/cm ³)	Grain bulk density (g/cm ³)	He Porosity (%)
4%	2.51	2.36	5.70
6%	2.50	2.37	5.19
22%	2.65	2.53	4.61
59%	2.67	2.61	2.48

2.1.3. Time-resolved acidic HFF penetration experiments

For each selected Wolfcamp shale sample, each core (apart the ‘initial’ shale core) was first reacted with 3 mL of 15% HCl (pH = −0.9) for 5 min in glass vials in order to simulate a typical acid spearhead. Pumping time for an acid spearhead is 5–10 min (FracFocus, <http://www.FracFocus.org>). This first stage recreates the contact time of the shale with a 5 min injection per the pumping schedule of the Marcellus well. Following this stage, 7 mL of HFF was added to the acid solutions from the first reaction step as would happen when injected pad fluid and slurry (injected after acid) displaced or mixed with the spearhead downhole. The acid spearhead mixed with HFF represents the final acidic HFF (as described in Table SM-1; pH = 1.4). Each core was thus immersed in 10 mL of final acidic HFF with 60 mL of air headspace in high temperature/pressure reactors (Parr Instruments, IL).

Reactors were sealed and pressurized with N₂ gas to 65 bar, and then placed in an 80 °C oven (Renock et al., 2016) resulting in a final pressure of 77 bar. These P/T conditions are supercritical for CO₂. Fig. 1 summarizes time-resolved experimental procedures and characterization techniques. To maintain continuity with an injection scenario, solutions

were not sparged of oxygen (Fig. 1). After each specified time interval (2 h, 2 days, and 7 days), an individual reactor was taken out of the oven and slowly degassed for 15 min, after which the reacted sample was immediately rinsed with Milli-Q water and dried under ambient conditions. Based on the pressure reading no gas leakage was noted during the reaction.

2.2. Elemental composition of bulk fluid over time

The pH of the bulk fluid from each selected Wolfcamp shale sample and the duration were measured using a glass combination pH electrode when the reaction fluid was completely cooled down to room temperature. After pH was measured, a portion of the aqueous solution was acidified (2% HNO₃) for measurements of Ca concentrations using Inductively Coupled Plasma Mass Spectrometry (ICP-MS).

2.3. Time-resolved synchrotron-based X-ray Fluorescence Microprobe (XFM) mapping of shales

After drying, the cylindrical core samples were cut perpendicular to the axis of the core, halfway between each end, yielding two shorter cores. The first half of each core was used for mapping the elemental and mineral distribution as a function of immersion time in the acidic HFF.

Bromide (Br), calcium (Ca), and silicon (Si) XFM maps were measured from the cut surface (HFF-shale interface) at ambient temperature on Beamline 2–3 at the Stanford Synchrotron Radiation Lightsource (SSRL, SLAC National Accelerator Laboratory, Menlo Park, CA). The XFM signal from the polished cut surfaces was recorded at 13,500 eV (optimized for Br) using a single element Hitachi vortex 90EX detector, with 50 mm area. Measurements were performed at room temperature. The angle subtended by the incident beam, sample, and

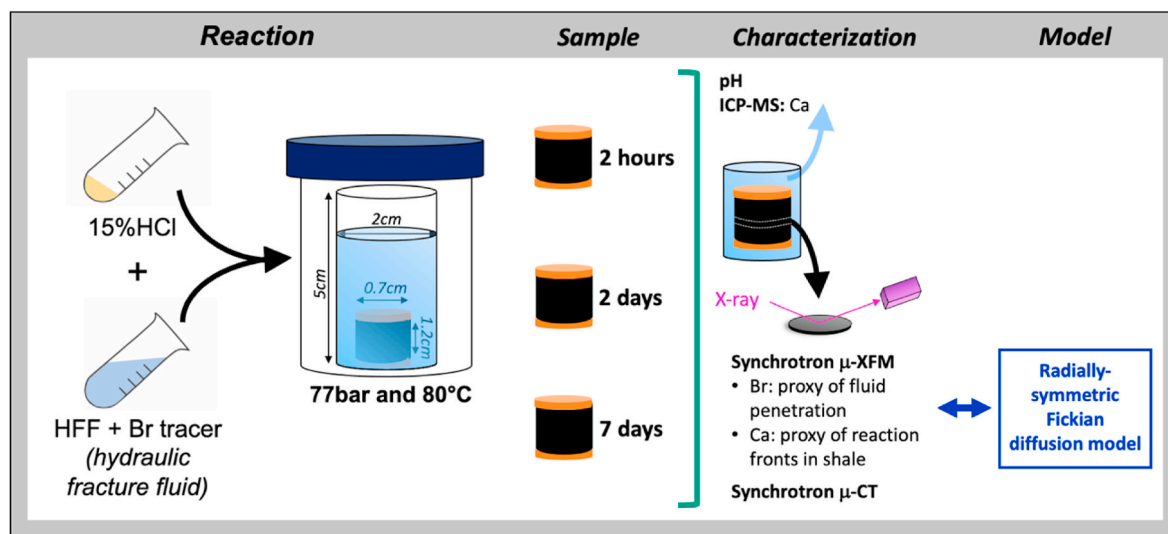


Fig. 1. Illustration of time-resolved experimental procedures and characterization techniques. 15% HCl and Br-doped hydraulic fracture fluid (HFF) form together the acidic (pH = 1.4) HFF. These time-resolved acidic HFF penetration experiments were repeated under similar conditions for each selected Wolfcamp shale sample characterized by different calcite concentrations (Table 1).

detector was 90°, with the sample normally bisecting this arrangement. The map step size was 3 μm and the dwell time was 100 ms.

To facilitate comparison of samples and XFM maps, all samples had the same sample-to-detector distance. Br accumulated masses were estimated using SMAK software (Webb, 2011) by comparison with the fluorescence of a 50.5 μg/cm² CsBr reference. For the quantification process, the data were normalized to the incident beam intensity and corrected for the absorption of the shale matrix. The MicroAnalysis Toolkit of SMAK assumes that the sample is infinitely thin and does not include any correction for thickness. Due to similar thickness and density of the core along the regions of interest, we assume that the matrix effects of the sample are constant along the map. The Br accumulated masses are thus comparable along each profile.

Si release from silicate dissolution is slow under our reaction conditions and not expected to result in a Si-depleted zone at the HFF-shale interface during 7 days of reaction. Consequently, Si XFM maps were compared with Ca XFM maps to deduce the spatial extent of Ca depletion.

2.4. Time-resolved synchrotron-based μ-CT images of shales

The second half of each shale core was used to map porosity change in the sample matrix using synchrotron-based transmission micro-computed tomography (μ-CT) on SSRL Beamline 2-2. Each data set consists of 360 projections, each of which were 0.15s in duration, during a 180° revolution. Data analysis and processing were done using Fiji software (Schindelin et al., 2012).

2.5. Modeling porosity and tracer transport

Reactive transport modeling was performed to evaluate if accumulation of bromide mass in the shale matrix, observed in the XFM maps (*vide infra*), was quantitatively consistent with enhancement of porosity due to calcite dissolution. We adopted the approach of Li et al. (2020) and used the open source CrunchFlow software (Steeffel et al. 2015). As demonstrated by Li et al. (2019b), this model can accurately simulate 1-D reactive transport in a water-saturated domain across a fluid-shale interface and within the shale matrix. This model simplifies the shale matrix system such that we may specifically address mass balance between calcite solubilization and bromide accumulation. The intent here was to use the previously developed model (Li et al., 2019b) suitable for these shale samples to verify whether the extent of calcite dissolution necessary to interpret our experimental data is feasible given the time-scale and initial and boundary conditions of the experiments. Under real conditions, carbonate solubilization also promotes the formation of CO₂ gas. Because there is no physical advection of the gas and no effusion included in models like CrunchFlow, Geochemist's Workbench, or other typical reactive transport models, the only accounting for CO₂ gas generation is through Henry's Law, which uses an equilibrium between the CO_{2(aq)} and CO_{2(g)} phases. We do not seek a direct representation of two-phase transport, CO₂ generation, or countercurrent flow.

In the single-phase model, we used diffusion as a proxy for the delivery of HCl and bromide across the fluid-shale interface and into the shale interior. Thus, the diffusion coefficient used here is an effective parameter for a combination of diffusion and capillary imbibition. The propagation of Br and acidic fluid through space and time into the core is quantified using the expression

$$\frac{\partial Br}{\partial t} = \frac{\partial}{\partial r} \left[RD_{eff} \frac{\partial Br}{\partial r} \right] \quad (\text{Eq. 1})$$

with an effective diffusion coefficient, D_{eff} (cm²/sec). The model domain is 1D and has a radius of 5 cm from rim to center, discretized into 500 cells of 0.01 cm each, consistent with the prior Li et al. (2019b) model but here updated to radial coordinates appropriate to a long circular cylinder where endcaps are negligible. The initial porosities of each

studied Wolfcamp shale sample are updated in each simulation to match the values measured for these shales (Table 2). The initial condition of the model is a fluid saturated core (corresponding to instantaneous imbibition of the fluid phase) with Br mass of zero across the shale matrix domain, with the left boundary pinned to an elevated Br concentration representing the surrounding fluid at the point of initial immersion. Acidity of the fluid (pH = 1.4) initially present within the shale is rapidly neutralized, and continued solubilization of calcite is largely restricted to a small area at the fluid-shale interface where acidity continues to be supplied by the surrounding fluid.

The model advances forward in time and calculates the solubilization of carbonate (represented as calcite) in the solid matrix. The remainder of the solid-phase mineralogy is represented as nonreactive quartz. Four different carbonate contents were simulated, including 4, 6, 22, and 59% of the total solid phase. These values correspond to the measured calcite contents for our shale samples (Table 1). In each simulation, calcite was allowed to dissolve following a first-order reversible transition state theory (TST) rate expression:

$$R = kA \left(1 - \frac{Q}{K_{eq}} \right) \quad (\text{Eq. 2})$$

where the overall dissolution rate (R) is the product of a rate constant (k), the mineral surface area (A), and the departure from equilibrium, calculated as the ratio of the ion activity product (Q) and the equilibrium constant for the appropriate temperature (K_{eq}). For these simulations, calcite rate parameters are identical to those used in Li et al. (2019b), consisting of a rate constant of 10⁻⁵ mol/m²/s, a starting surface area of 1.0 m²/g, and an equilibrium constant of 10^{1.8487}. These kinetic parameters (rate constant and surface area) were constrained in Li et al. (2019b) using time series aqueous chemical data from batch reaction experiments involving exposure of Marcellus and Eagle Ford cores to HFF. The resulting evolution of pH and dissolved calcium with time constrains the parameterization of calcite dissolution specific to these experimental conditions and samples. All aqueous species activities were calculated using an extended Debye-Huckel model, and the complete pH and calcite equilibria were included as reported in Li et al. (2019b) for a similar shale diffusion experiment.

The result is a model that tracks the progression of Br⁻ tracer and consumption of acid through solubilization of carbonate (more specifically calcite), creating new porosity within the shale along a reactive front governed by the balance between Eq. (2) and diffusive transport. In addition to the dissolution rate (calculated from Eq. (2)), the X-ray mapping returns the $\frac{\partial Br}{\partial r}$ profile at a given time, and thus the effective diffusion coefficient (D_{eff}) is adjusted to recover the observed profile at the appropriate time interval. The modeled mass of Br tracer that enters the shale interior is thus impacted by both diffusion and the pore volume available as the carbonate dissolves. Thus, in our model, carbonate (*i.e.*, calcite) dissolution and the advance of the reactive front govern the overall mass of Br that can occupy the shale interior.

3. Results

3.1. Fluid-rock interaction in shales as a function of the calcite content

For each Wolfcamp shale sample, dissolved Ca concentrations in the bulk fluid and pH increase (Fig. 2), indicating that imbibition of HFF led to the dissolution of carbonate as expected. Overall, the concentration of dissolved Ca and pH in bulk fluid increased with calcite content in the shale matrix. However, some anomalies exist. For example, the dissolved Ca concentration in the bulk fluid is higher for the 6%-calcite shale than the 22%-calcite shale after 2 days of immersion of the shale in acidic HFF. In addition, pH in the bulk HFF increases faster for the 22%-calcite shale than for the 59%-calcite shale, but dissolved Ca concentration and pH reached similar values after 7 days of immersion. These anomalies are the consequences of the complexity of natural samples

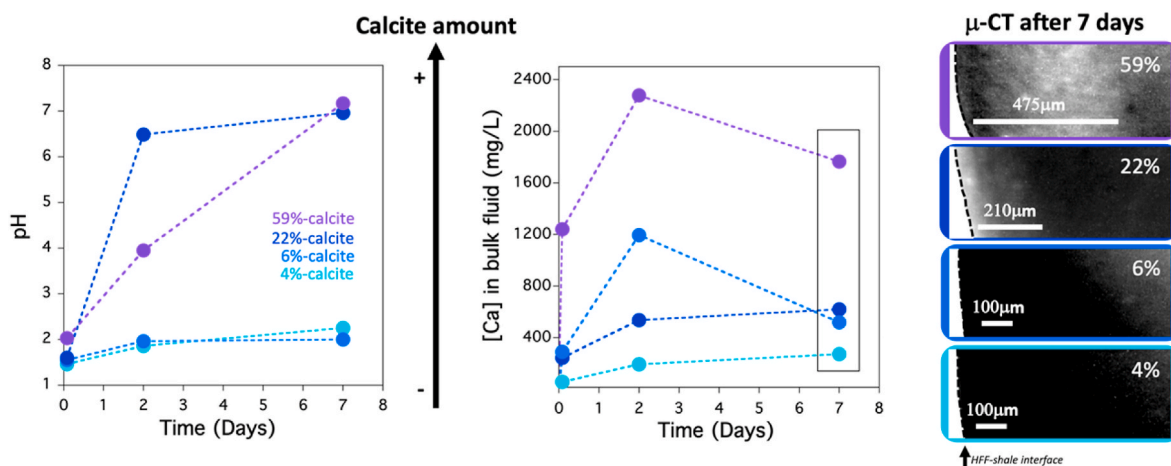


Fig. 2. pH (left) and dissolved Ca concentration (middle) in the bulk fluid during the immersion of Wolfcamp shale in acidic HFF. Synchrotron-based transmission μ -CT maps of Wolfcamp shale after 7 days of immersion in acidic HFF (right). Because shale samples are too thick, X-rays do not transmit through the shale, and the μ -CT maps appear black. The increasing frequency of white pixels at the HFF-shale interface is attributed to increasing porosity. During immersion of Wolfcamp shale samples in acidic HFF, the porosity of shales increases beginning from the HFF-shale interface. With increasing porosity, X-rays finally pass through the shale samples and white pixels appear.

(mainly attributed to the differences in heterogeneity from one sample to another).

3.2. Mapping HFF transport in shales as a function of the calcite content

Synchrotron-based X-ray chemical imaging penetrates below surfaces, which scanning electron microscopy (SEM) cannot do. As a result, synchrotron-based X-ray chemical imaging can be used to detect chemical changes at micrometer length scales at lower detection limits than SEM.

Potential Br^- sorption is mainly driven by decreasing pH ($\text{pH} < 7$) and the presence of clay minerals (Goldberg and Kabengi, 2010). In experiments with Wolfcamp shales, that represent a large variability of clay content (Table 1), we do not observe such behavior (See §2.1.2 and Figure SM-1). Instead, we concluded that Br^- behavior is not influenced by sorption in these experiments. Mapping of the Br distribution (aqueous phase) in the shale reveals thus the advancement of imbibing HFF into the shale. As the shale pores become enlarged due to calcite dissolution, the amount of bromide that enters the matrix increases. These changes are best interpreted in terms of mass accumulation rather than concentration changes. Consequently, we hereafter refer to mass accumulation profiles for the bromide data. Because samples mapped are dried, Br is presumably presents in the samples as bromide salts. Indeed, free bromine does not occur in nature; instead, bromine is usually found in the form of mineral halide salts (Brown, 2014).

Fig. 3 shows extracted profiles from time-resolved XFM maps of the Br^- tracer distribution in the matrix of Wolfcamp shales after immersion of the shale in acidic HFF. In comparison to the imbibed Br tracer, all shales contain a very low background signal of Br (herein referred to as initial; Fig. 3 and SM-2). The accumulated mass profiles of Br (in $\mu\text{g}/\text{cm}^2$) from the HFF-shale interface to the center of the core indicate that Br^- imbibition reaches the center of the core in less than 2 h regardless of the matrix calcite content (Fig. 3 and Figure SM-2). The XFM profiles show that the accumulated Br mass at any point in the core increased from 2 h to 7 days. This behavior indicates that over time an increasing fraction of pores was saturated with Br-rich HFF and/or that their average volume increased (*i.e.*, due to calcite dissolution) over 7 days. In addition, the profiles show that the accumulated Br mass is systematically higher at the HFF-shale interface than in the interior of the shale for any time of reactivity, even at 2 h of reactivity (first time step). After 7 days of immersion in acidic HFF, the accumulated Br mass at the HFF-shale interface increases as a function of calcite content in the shale

matrix from $239 \mu\text{g}/\text{cm}^2$ for the 4%-calcite shale sample to $322 \mu\text{g}/\text{cm}^2$, $363 \mu\text{g}/\text{cm}^2$, and more than $1300 \mu\text{g}/\text{cm}^2$ for the 6%-, 22%-, and 59%-calcite shale samples, respectively (Table 3).

3.3. Mapping chemical reaction fronts in shale matrix

XFM mapping was used to measure the distribution of Ca and can serve as a proxy for the distribution of calcite and other Ca-bearing minerals (Figure SM-3 and Fig. 3). Mapping of Ca (solid phase) reveals advancement of the (slower moving) calcite dissolution fronts at a fine spatial scale (*e.g.*, micrometers). We can neglect the signal contributed from dissolved $\text{Ca}_{(\text{aq})}^{2+}$ because of the low porosity ($< 6\%$) and orders-of-magnitude lower dissolved Ca concentration as compared to the shale matrix. Because the profiles of Ca are discussed qualitatively to interpret the Br accumulated mass, the Ca fluorescence intensity is not converted into mass.

The observed increase in the accumulated mass of Br in the pores at the HFF-shale interface between 2 h and 7 days of immersion in acidic HFF was accompanied by a decrease in Ca mass that was most pronounced at the HFF-shale interface, where the most acidic conditions will prevail in the matrix. Concomitant with the increase of the accumulated Br, calcite was dissolved at the HFF-shale interface. This behavior intensified as a function of calcite content in the shale matrix (50% and 70% loss for the 4%- and 6%-calcite shale samples, and 100% loss for the 22%- and 59%-calcite shale samples, after 7 days of immersion in acidic HFF). This behavior was increasingly restricted to the HFF-shale interface as the amount of calcite increased (1.5 mm for the 4%-calcite samples, 1.2 mm for 6%-calcite samples, and 0.4 mm for the 22%-calcite and 59%-calcite samples).

Inspection of the XFM maps for Br and Ca (Figure SM-2 and SM-3) shows that for the low calcite content cores, Br mass and Ca fluorescence distributions are relatively uniform, with gradients developed perpendicular to the HFF-shale interface. No structures are evident that would indicate channeling of CO_2 effluxing across the interface. The incident X-ray beam penetrates tens of micrometers into the matrix. Consequently, we would expect to see channels present not only on the surface of the core slices (cut following completion of the experiment), but also below the surface. In cores with greater calcite content, the Br and Ca maps contain low-concentration discontinuities and patches approximately $50\text{--}100 \mu\text{m}$ in size. It is plausible that these patches represent locally higher permeability regions where effluxing CO_2 helps to prevent HFF imbibition.

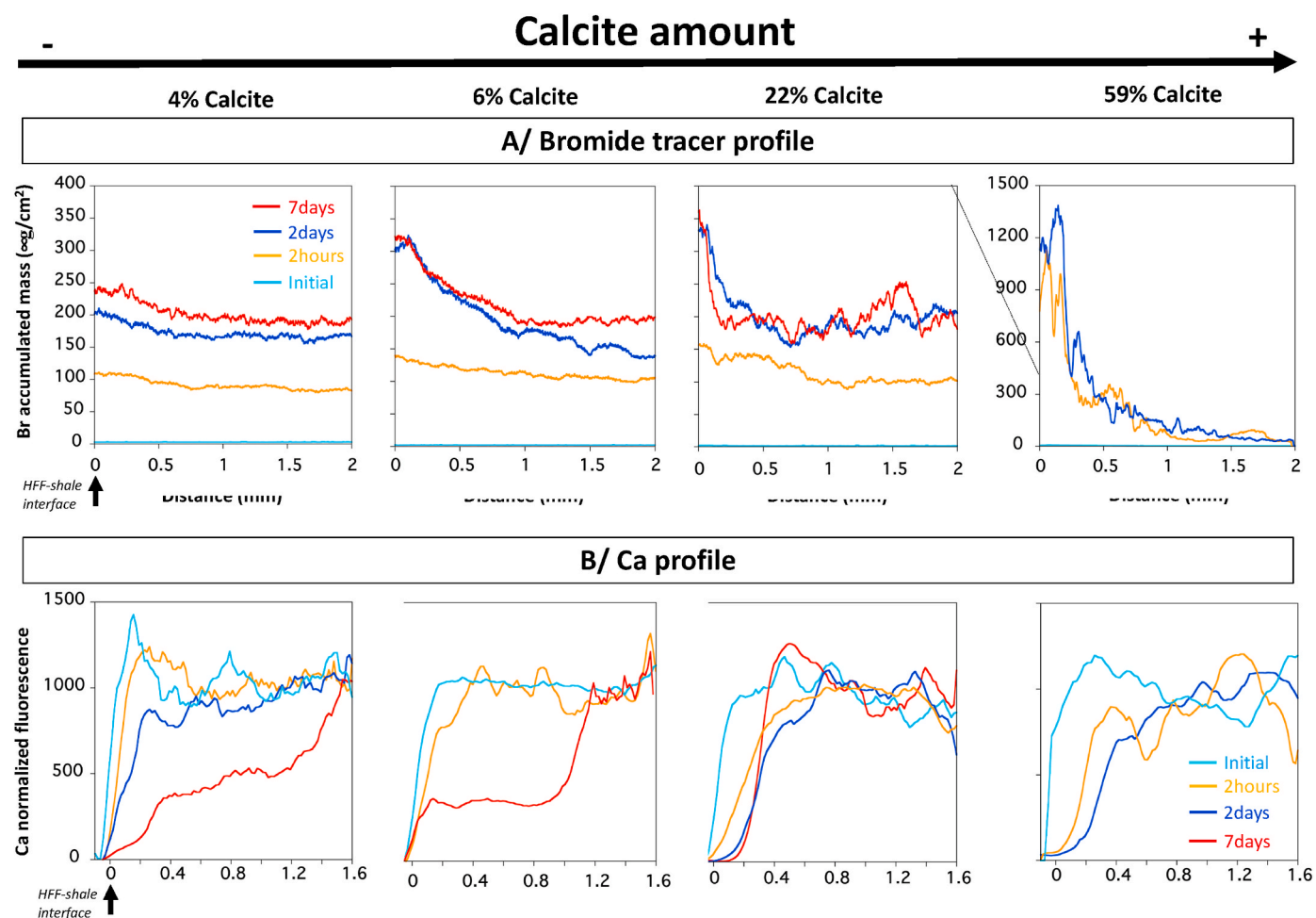


Fig. 3. Top: Br accumulated mass profiles, from the HFF-shale interface to the center of the core, extracted from the synchrotron-based μ -XFM maps (Figure SM-3) of Wolfcamp shales before (= *initial state*) and after 2 h, 2 days, and 7 days of immersion in acidic HFF.

Bottom: Ca fluorescence profiles, from the HFF-shale interface to the center of the core, extracted from the synchrotron-based μ -XFM maps (Figure SM-4) of Wolfcamp shales before (= *initial state*) and after 2 h, 2 days, and 7 days of immersion in acidic HFF. The Ca profiles were first smoothed to ignore the signal from Ca-rich spots. Each profile was normalized for comparing the Ca-loss spatial extent.

Due to major dissolution of calcite in the 59%-calcite Wolfcamp shale sample after 7 days of immersion in acidic HFF, the first 300–500 μ m from the HFF-shale interface were extensively damaged showing strong surface irregularity. This topographic irregularity between the shale surface, beam, and detector, posed significant challenges for mapping the Br and Ca distributions.

Table 3

Experimentally measured Br mass accumulated at the HFF-shale interface compared to modeled Br mass accumulated at the Fluid-shale interface (h: hour, D: day).

Sample ID	Experimentally measured Br mass accumulated at the HFF-shale interface ($\mu\text{g}/\text{cm}^2$)			Modeled Br mass accumulated at the fluid-shale interface ($\mu\text{g}/\text{cm}^2$)		
	2 h	2D	7D	2 h	2D	7D
4%-Calcite	111	205	239	149	208	223
6%-Calcite	140	303	322	116	205	228
22%-Calcite	157	333	363	122	449	536
59%-Calcite	917	1221	1300	110	1009	1235

Transmission μ -CT images of shale collected before and after 2 h, 2 days and 7 days of immersion of the shale in acidic HFF are displayed in Figure SM-4 and Fig. 2. Before immersion of the shale in acidic HFF, shale samples were too thick for X-rays to transmit through the shale, and the transmission μ -CT images appear black (Figure SM-4). During immersion of a shale sample in acidic HFF, mineral dissolution theoretically increases the porosity and consequently increases the ability of X-rays to transmit through the shale. Once the porosity increases

sufficiently for X-rays to pass through the shale within the pores of the illuminated rock matrix volume (pixel diameter of 0.567 μ m), μ -CT images show lighter-colored pixels. The increasing area of lighter pixels is thus attributed to increasing porosity (Fig. 2). Transmission μ -CT images of shale collected during the first 7 days of immersion of the shale in acidic HFF show that calcite-poor shales (the 4%- and 6%-calcite samples) are still opaque to X-rays after 7 days (Figure SM-4 and Fig. 2). In contrast to the calcite-poor shale, the HFF-shale interfaces of calcite-rich shales (the 22%- and 59%-calcite samples) became partially transparent to X-rays after only the first 2 h of immersion in acidic HFF (Figure SM-4 and Fig. 2). The spatial extents of the increasing porosity from the HFF-shale interface of calcite-rich shales (the 22%- and 59%-calcite samples), observed from transmission μ -CT images, corroborate those observed with Ca mass loss from Ca XFM maps. The μ -CT and Ca mass loss XFM images of the 22%-calcite shale are compared in Figure SM-5 as an example. Furthermore, the area that transmits X-rays seems to spatially extend deeper into the matrix for the 59%-calcite shale sample (\sim 475 μ m) than the 22%-calcite shale sample (\sim 275 μ m). Thus, transmission μ -CT images suggest that imbibition of acidic HFF promotes accumulation of increasing porosity from the HFF-shale interface with higher amounts of calcite (Fig. 2). Thus, the higher calcite content, the more porosity increases into the matrix starting at

the HFF-shale interface.

3.4. Model of acidic fluid reactive transport as a function of the calcite content

We consider that each shale sample selected to provide a range of calcite contents may differ in their individual pre-reacted porosity. Therefore, each modeled profile is initiated from a specific porosity value corresponding to the initial measured value for that core. Before immersion of the shale in acidic fluid (referred to as initial), we observed that He porosity is inversely correlated with calcite content (Table 2). The mineral volumes (*i.e.*, 1-porosity) are then divided into the appropriate calcite content and the remaining solid phase, that is represented by a nominally unreactive silicate mineral (quartz). The evolution of porosity with distance from the fluid-shale interface to the center of the Wolfcamp cores is then simulated on a case-by-case basis using the appropriate initial conditions (Fig. 4). All simulations demonstrate a loss of calcite content, primarily near the rim of the core, as a function of time. As a consequence, the profiles indicate that porosity systematically increases at the fluid-shale interface over time for all calcite contents (Fig. 4). The corresponding mass of Br^- tracer as a function of distance and time is then a product of the static concentration of Br^- in the fluid phase and the evolving volume of open pore space (the porosity) in each grid cell in the model (Fig. 4).

The trend of modeled accumulated tracer mass shows close agreement with the experimental results (Figs. 4 and 5) in two ways: (i) accumulated tracer mass increases at any point in the core from 2 h to 7 days; and (ii) accumulated tracer mass increases at the fluid-shale interface as a function of the calcite content. This close agreement between modeled and observed Br^- tracer distribution serves as a key indication that the simulations are successfully representing the general

behavior of the experimental system (Fig. 5). An exception to this statement is that the tracer mass modeled on short-time scales (after 2 h of immersion of the shale in acidic fluid) differs strongly from the experimentally measured accumulated Br mass, suggesting that the model under-evaluates the accumulation of Br in the pores at the HFF-shale interface at a very early time when HFF imbibition is rapid.

Critically, the increase in porosity through space and time for all simulations maintains the same representative calcite stoichiometry, the same starting surface area, and the same rate parameters for calcite dissolution (see ‘Material and Analytical Procedures’ section). The only differences between simulations are the initial calcite volume fraction and initial porosity for each core. We are thus able to contrast the secondary porosity developed at the fluid-shale interface as a function of the calcite content (Fig. 5). The increase in porosity at the edge of the fluid-shale interface is dependent significantly on the calcite content of the matrix. For the 59% calcite sample, the porosity increases by approximately 50% in 7 days, whereas the 4% calcite sample only accommodates a small change. This difference in porosity generation at the edge of the fluid-shale interface is inversely correlated with the depth of porosity generation into the interior of the shale. To quantify this inverse relationship, we take the derivative of the porosity distribution as a function of radial distance into the interior of the core and consider the maximum alteration depth at which the gradient reaches zero for any given model. The result indicates that the calcite-rich Wolfcamp shale samples restrict the depth of alteration to a shallower zone along the fluid-shale interface, whereas the calcite-poor samples show a much deeper extent of alteration (Fig. 5). This result is consistent with the experimental profiles of the Ca mass, which suggest that the spatial extent of the Ca mass loss is more confined near the HFF-shale interface when the shale is rich in calcite (Fig. 3).

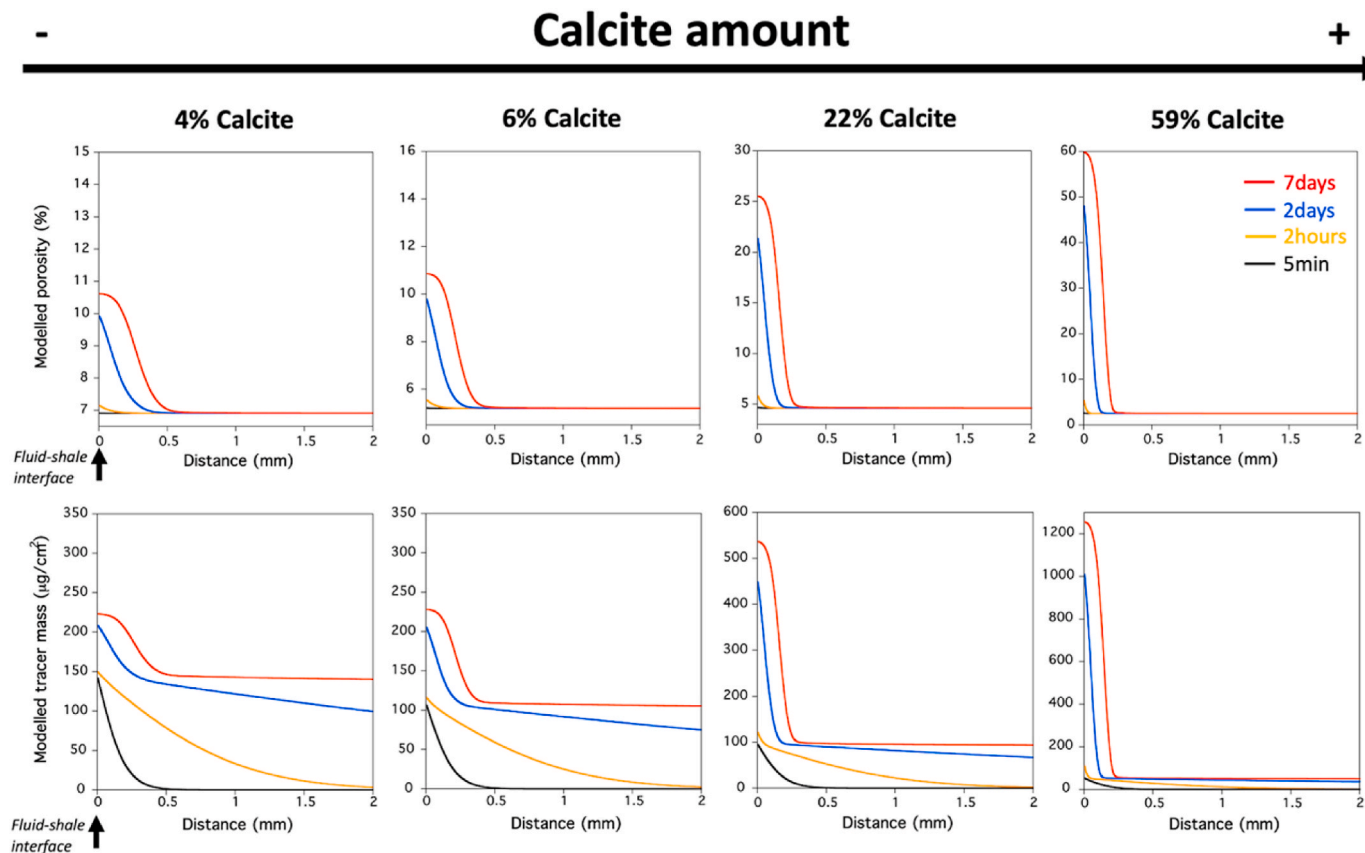


Fig. 4. Simulated porosity (top) and tracer mass profiles (bottom) in the pore fluid at the fluid-shale boundary (left side of plots) after 5 min, 2 h, 2 days, and 7 days of immersion in acidic fluid. The model results are expressed in radial coordinates.

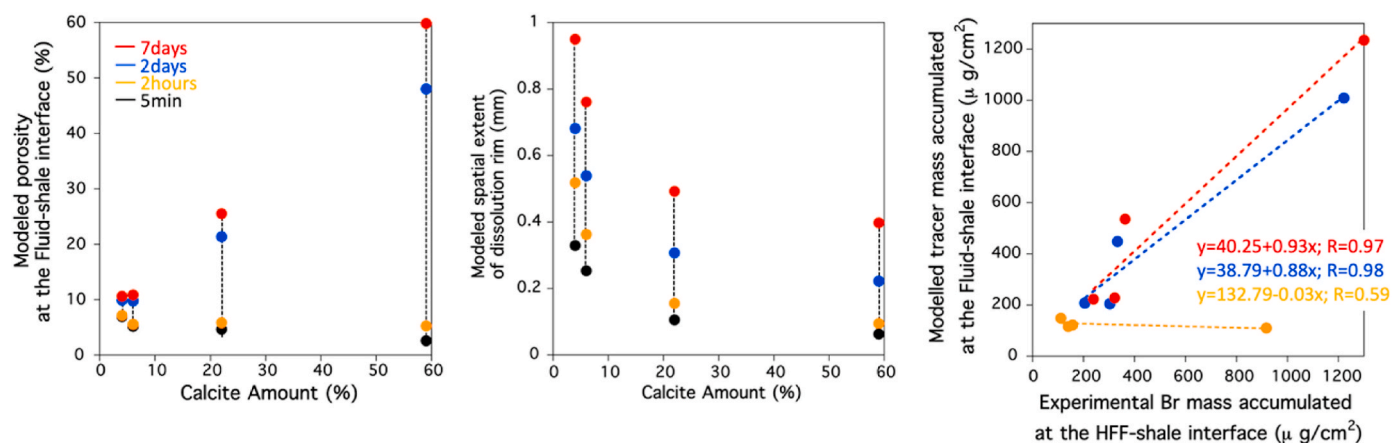


Fig. 5. Modeled porosity at the Fluid-shale interface (0 μm depth; left) and spatial extent of the modeled increasing porosity from the Fluid-shale interface (middle) in Wolfcamp shales after 5 min, 2 h, 2 days, and 7 days of immersion of the shale in acidic fluid. The model results are expressed in radial coordinates. The porosities of Wolfcamp shales, measured before immersion in acidic fluid, were adopted in the model (Table 2). The model data corroborates with the experimental data and suggest that porosity at the Fluid-shale interface increases proportionally with the amount of calcite. The spatial extent of alteration decreases proportionally with the amount of calcite.

Then, the modeled Br mass that accumulated at the Fluid-shale interface (0 μm depth) was compared to the maximum accumulated Br mass measured experimentally along the first 50 μm from the HFF-shale interface (right). The values are reported in Table 3 for better comparison. Each linear fit representing the relationship between model and experimental accumulated Br mass, after 2 h, 2 days, and 7 days of immersion of the shale in acidic fluids, are designated with a colored dashed line (right). Equations corresponding to each linear fit are also shown in the figure.

4. Discussion

4.1. Porosity enhancement and fluid mass accumulation

We return to our guiding question: does imbibition occur on a timescale concurrent with porosity alteration via dissolution calcite? The bromide tracer provides a signal that can be used to track the advancement of solute within the shale matrix as well as the expanding alteration zone in which porosity enhancement occurs (Li et al., 2019a; Gundogar et al., 2021). The bromide profiles presented in Fig. 3 show that within 2 h of reaction, bromide had imbibed throughout the shale core. The relatively flat bromide mass accumulation profiles (*i.e.*, extending from the HFF-shale interface to the center of the core) after just 2 h of reaction are consistent with minimal alteration of porosity. This observation leads to the conclusion that initial acid HFF imbibition due to capillarity is fast in comparison to calcite dissolution. Thus, during the initial 120-min period, acidic HFF was transported over a distance of 3.5 mm to the center of the core with relatively minor alteration to soluble minerals.

In contrast, during the ensuing 7-day period, shale porosity was significantly enhanced in the zones where HFF had already imbibed. One possible explanation for this behavior is that acid HFF transported into the shale during the initial fast imbibition step subsequently reacted with the shale matrix to create the observed porosity. If this mechanism was indeed influential, then the spatial distribution of the enhanced porosity (*i.e.*, during the 2 h to 7 d interval) should mimic the profile of the initial imbibed bromide. That is, porosity enhancement should be relatively constant (flat profile) with depth into the core. However, this behavior was not observed. Instead, the porosity is sharply enhanced in immediate proximity to the HFF-shale interface, with the extent of enhancement decreasing sharply with increasing distance away from the interface. This general pattern of porosity modification is consistent with ongoing transport of acidic HFF into the matrix with concurrent calcite dissolution (Fig. 3) and ongoing release of Ca^{2+} into the HFF (Fig. 2). In support of this conceptual model, reactive transport simulations (Fig. 4) suggest that porosity enhancement after 2 h cannot be explained solely by the acidity of HFF initially present in the shale interior. Rather, an ongoing multistep process must be occurring, that includes: (i) Opening of pores following the initial imbibition step; (ii) Progressive imbibition of acidic HFF at slower rates to fill the newly

opened pores; and (iii) Dissolution of calcite concurrent with ongoing imbibition to create additional porosity. This process then cycles through steps (ii) and (iii) as the HFF enters the matrix.

Between 2 h and 7 days, the timescale of calcite dissolution governs the opening of pore space and hence the timescale over which more HFF moves into the shale matrix. Consequently, porosity enhancement could proceed concurrently with imbibition, leading to the development of well-defined reaction fronts. Thus, we observed an initial fast transport regime (*i.e.*, Damköhler number $\ll 1$), that does not produce reaction fronts with a subsequent regime of concurrent imbibition and dissolution consistent with rate-limited conditions.

Some CO_2 produced by dissolution of calcite is expected to have escaped from the matrix into the surrounding fluid. However, no structures are evident to indicate that CO_2 was persistently flowing out the channel-like structures, thus counteracting HFF penetration. Indeed, the geochemical reaction fronts are well developed, with no clear indications that effluxing CO_2 significantly disrupts the development of geochemical reaction fronts. In the higher calcite content cores, effluxing CO_2 may have preferentially escaped through low-bromide content zones that are detected in the bromide maps. Future work will focus on understanding how the escaping gas interferes with or modifies the reactive transport process.

4.2. Control on spatial extent of imbibition and geochemical reaction fronts

One intriguing question relates to the progressive sharpening and shallowing of the reaction front and altered region with increasing calcite content. Despite significantly lower initial porosity in the calcite-rich shales, the experimental and model results indicate that the greatest enhancement of porosity occurred in shales with higher calcite contents, specifically in the region immediately proximal to the HFF-shale interface (Table 2 and Fig. 5). Moreover, Ca^{2+} release to solution was greater in calcite-rich samples. However, despite the calcite dissolution is greater in shales with higher calcite contents, the spatial extent of pore alteration from the HFF-shale interface to the center of the core is inversely proportional to the amount of calcite in the matrix (Fig. 5).

Advancement of the acidic HFF front into the shale core causes secondary porosity to increase over time in the direction of the core interior. Concurrently, dissolution of calcite consumes acidity, causing

pH to increase. The overall rate of calcite dissolution and acid neutralization increases in proportion to the total surface area of calcite present (cf., Eq. (2)), which in turn increases with calcite mass percent. Consequently, in shales with more abundant calcite, imbibing acidic HFF are neutralized more quickly during transport into the matrix. The Ca XFM maps (Fig. 3 and SM-3) and model simulations (Fig. 5) reflect this behavior, *i.e.*, the decrease in Ca mass in response to calcite dissolution is the most intensive but also the most restricted at the HFF-shale interface in calcite-rich shales. The extent of advancement of the acidic HFF and the corresponding dissolution (porosity enhancement) front from the HFF-shale interface to the center of the core are consequently inversely related to the amount of calcite in the matrix. This behavior creates the well-defined reaction fronts outlined in the preceding section.

Recent model studies (Li et al., 2020) have concluded that imbibed acidic HFF are slowly neutralized in low-carbonate shale matrices (*i.e.*, over weeks to months), whereas the process takes hours to days in a high-carbonate shale. These earlier studies did not have access to time-resolved data, and consequently the simulations of short timeframe processes were poorly constrained. However, the current study generally supports these earlier model studies. Br mass accumulation and the Ca loss profiles for the low-calcite samples were still evolving between 2 and 7 days of reaction (Fig. 3). These observations imply that matrix dissolution was still active at that point in time. In contrast, the major proportion of the Ca loss (*i.e.*, calcite dissolution) from the calcite-rich shales (the 22%- and 59%-calcite samples) occurred within the first 2 h of immersion (Fig. 3).

4.3. Impact on matrix mineral scale formation

pH is one of the main controlling factors for the formation of secondary minerals, such as sulfates (Vankeuren et al., 2017; Jew et al., 2019) and iron oxides (Jew et al., 2017). The pH profile in the shale determines the location and overall amounts of the secondary minerals, which in turn moderate porosity and permeability of the shale matrix. Indeed, while low pH drives mineral dissolution, pH neutralization causes mineral precipitation. Slow neutralization of pH in carbonate-poor shale promotes slower and less extensive mineral scale precipitation rates. In contrast, the rapid and extensive calcite dissolution (a few hours) confined at the HFF-shale interface in the carbonate-rich shale (Fig. 3) promotes rapid neutralization in the shale matrix pores at the HFF-shale interface, which could foster rapid precipitation (a few hours) of secondary minerals in the shale matrix. Consequently, the chemical and physical properties (permeability and porosity) of the HFF-shale interface along fractures of the carbonate-rich shales could change concomitantly with acidic HFF imbibition. For example, the formation of metal (Fe, K, Ti, Cr, Mn, and Ni) enriched rims extending several hundred μm into the shale matrix were promoted in the carbonate-rich shale over timescales of approximately 2 h (Noël et al., 2020).

Rapid calcite dissolution confined to the HFF-shale interface further promotes the development and erodibility of the altered layer on the fracture surfaces as proposed by the model of Deng et al. (2017). Thus, high calcite concentrations promote dissolution of fracture surfaces and dislodging of relatively inert particles such as quartz, clays, organic matter, or even pyrite (Newell and Carey, 2013; Wu and Sharma, 2017; Kreisserman and Emmanuel, 2018). The release of fine particles could migrate and clog pore necks of microfractures or, conversely, could result in the transport of potential contaminants associated with these particles (Qajar et al., 2013; Kreisserman and Emmanuel, 2018).

5. Conclusion

In the context of hydraulic stimulation of unconventional reservoirs, the overall rates of calcite dissolution approach those of acidic HFF transport (*i.e.*, Damköhler number ~ 1) and result in the increase of the accessible porosity within the reaction front on a timescale coincident

with HFF imbibition. Under these conditions, well-defined reaction fronts can develop. In this study, we demonstrated that the relative abundance and spatial distribution of calcite are master variables controlling the spatial extent and rate of matrix alteration. These master variables also control the pH and chemical saturation state of the HFF progressing into the matrix, with important consequences for mineral scale precipitation. Consequently, calcite content of the fractured reservoir largely could contribute to the efficiency in subsurface reservoir stimulation.

Similarly, several recent studies provide evidence that multiple fluid-rock chemical reactions occur concurrently with imbibition of injected fluids. For example, Burnside et al. (2019) found that the majority of mineral dissolution due to hydraulic stimulation of geothermal reservoirs occurs during the first 24 h after the injection phase, while Menefee et al. (2020) detected precipitation of secondary minerals within 10 min following fresh shearing in shales. In addition, Zhou et al. (2016) found that mesoscopic damage to rock surface hardness in shales occurred during the first hour of imbibition of stimulation fluids in the shale matrix. As highlighted by our study, these rapid subsurface reservoir compositional/mineralogical alterations during stimulation fluid transport could impact the rate and composition of the fluid progressing into the matrix, and thus the efficiency of subsurface reservoir stimulation. This short-time scale feedback between HFF transport and reactive compositional/mineralogical alteration of pore structure should consequently focus greater attention on optimizing engineering technologies such as (un)conventional hydrocarbon production, geothermal energy production, CO₂ sequestration, and nuclear waste disposal while minimizing environmental damage such as excessive water use (Kondash et al., 2018).

Declaration of competing interest

The authors declare that they have no known competing financial interests or personal relationships that could have appeared to influence the work reported in this paper.

Data availability

Data will be made available on request.

Acknowledgments

This research was funded by the Center for Mechanistic Control of Water-Hydrocarbon-Rock Interactions in Unconventional and Tight Oil Formations (CMC-UF), an Energy Frontier Research Center funded by the U.S. Department of Energy (DOE), Office of Science under BES Award DE-SC0019165. The Stanford Synchrotron Radiation Lightsource (SSRL) and SLAC National Accelerator Laboratory are supported by the U.S. DOE and by the National Institutes of Health, National Institute of General Medical Sciences (including P41GM103393). We thank Dr. Adam Jew for his assistance in conducting the experiments. We gratefully acknowledge Dr. Sam Webb, Dr. Sharon Bone, and the technical staff at SSRL for their technical support during the X-ray fluorescence mapping measurements. We also acknowledge Dr. Johanna Nelson, Dr. Yechuan Chen, and the technical staff at SSRL for their technical support during the Synchrotron-based transmission micro-tomography. The authors further thank Dr. Guangchao Li (Stanford University) for his help in the ICP analyses.

Appendix A. Supplementary data

Supplementary data to this article can be found online at <https://doi.org/10.1016/j.apgeochem.2022.105542>.

References

- Abd, A.S., Elhafyan, E., Siddiqui, A.R., Alnoush, W., Blunt, M.J., Alyafei, N., 2019. A review of the phenomenon of counter-current spontaneous imbibition: analysis and data interpretation. *J. Petrol. Sci. Eng.* 180, 456–470.
- Beulke, S., Brown, C.D., Fryer, C.J., Beinum, W.V., 2004. Influence of kinetic sorption and diffusion on pesticide movement through aggregated soils. *Chemosphere* 57 (6), 481–490.
- Brown, D., 2014. In *Encyclopedia of Toxicology*, third ed.
- Burnside, N.M., Westaway, R., Banks, D., Zimmermann, G., Hofmann, H., Adrian, J., 2019. Rapid water-rock interactions evidenced by hydrochemical evolution of flowback fluid during hydraulic stimulation of a deep geothermal borehole in granodiorite: Pohang, Korea. *Appl. Geochem.* 111, 104445.
- Cai, J., Li, C., Song, K., Zou, S., Yang, Z., Shen, Y., Meng, Q., Liu, Y., 2020. The influence of salinity and mineral components on spontaneous imbibition in tight sandstone. *Fuel* 269, 117087.
- Deng, H., Voltolini, M., Molins, S., Steefel, C., DePaol, D., 2017. Alteration and erosion of rock matrix bordering a carbonate-rich shale fracture. *Environ. Sci. Technol.* 51 (15), 8861–8868.
- El-Maghraby, R.M., Blunt, M.J., 2013. Residual CO₂ trapping in Indiana limestone. *Environ. Sci. Technol.* 47 (1), 227–233.
- Evje, S., Hiorth, A., 2011. A model for interpretation of brine-dependent spontaneous imbibition experiments. *Adv. Water Resour.* 34 (12), 1627–1642.
- Gale, J.F.W., Elliott, S.J., Laubach, S.E., 2018. Hydraulic Fractures in Core from Stimulated Reservoirs: Core Fracture Description of HFTS Slant Core, Midland Basin, West Texas in Unconventional Systems in Unconventional Resources Technology Conference Proceedings, URTEC 2902624.
- Ganguly, S., Kumar, M.S.M., 2014. Analytical solutions for transient temperature distribution in a geothermal reservoir due to cold water injection. *Hydrogeol. J.* 22, 351–369.
- Ghane, E., Feyereisen, G.W., Rosen, C.J., 2019. Efficacy of bromide tracers for evaluating the hydraulics of denitrification beds treating agricultural drainage water. *J. Hydrol.* 574, 129–137.
- Goldberg, S., Kabengi, N.J., 2010. Bromide adsorption by reference minerals and soils. *Vadose Zone J.* 9, 780–786.
- Gundogar, A.S., Ross, C.M., Jew, A.D., Bargar, J.R., Kovscek, A.R., 2021. Multiphysics investigation of geochemical alterations in Marcellus shale using reactive core-floids. *Energy Fuels* 35 (13), 10733–10745.
- Hall, C., 2019. Capillary imbibition in cement-based materials with time-dependent permeability. *Cement Concr. Res.* 124, 105835.
- Haluszczak, L.O., Rose, A.W., Kump, L.R., 2013. Geochemical evaluation of flowback brine from Marcellus gas wells in Pennsylvania. *USA. Appl. Geochem.* 28, 55e61.
- Hammack, R., Harbert, W., Sharma, S., Stewart, B., Capo, R., Wall, A., Wells, A., Diehl, R., Blaushild, D., Sams, J., Veloski, G., 2014. An Evaluation of Fracture Growth and Gas/Fluid Migration as Horizontal Marcellus Shale Gas Wells Are Hydraulically Fractured in Greene County, Pittsburgh, Pennsylvania: NETL-TRS-3-2014; EPA Technical Report Series. U.S. Department of Energy, National Energy Technology Laboratory, Pittsburgh, PA), p. 76.
- Harrison, A.L., Jew, A.D., Dustin, M.K., Thomas, D.L., Joe-Wong, C.M., Bargar, J.R., Johnson, N., Brown Jr., G.E., Maher, K., 2017. Element release and reaction-induced porosity alteration during shale-hydraulic fracturing fluid interactions. *Appl. Geochem.* 82, 47–62.
- Jew, A.D., Dustin, M.K., Harrison, A.L., Joe-Wong, C.M., Thomas, D.L., Maher, K.M., Brown Jr., G.E., Bargar, J.R., 2017. Impact of organics and carbonates on the oxidation and precipitation of iron during hydraulic fracturing of shale. *Energy Fuels* 31, 3643e3658.
- Jew, A.D., Li, Q., Cercone, D., Brown Jr., G.E., Bargar, J.R., 2019. A New Approach to Controlling Barite Scaling in Unconventional Systems in Unconventional Resources Technology Conference Proceedings, URTEC-2019-512-MS.
- Kastrinos, J.R., Chiasson, A., Ormond, P., 2019. Estimating groundwater heat exchange in a standing-column well by injection of a bromide tracer. *Geothermics* 82, 121–127.
- Kondash, A.J., Lauer, N.E., Vengosh, A., 2018. The intensification of the water footprint of hydraulic fracturing. *Sci. Adv.* 4 (8), eaar5982.
- Kreisserman, Y., Emmanuel, S., 2018. Release of particulate iron sulfide during shale-fluid interaction. *Environ. Sci. Technol.* 52 (2), 638–643.
- Krevor, S.C.M., Pini, R., Zuo, L., Benson, S.M., 2012. Relative permeability and trapping of CO₂ and water in sandstone rocks at reservoir conditions. *Water Resour. Res.* 48, W02532.
- Lester, Y., Ferrer, I., Thurman, E.M., Sitterley, K.A., Korak, J.A., Aiken, G., Linden, K.G., 2015. Characterization of hydraulic fracturing flowback water in Colorado: implications for water treatment. *Sci. Total Environ.* 512e513, 637e644.
- Li, K., Horne, R.N., 2010. Method to evaluate the potential of water injection in naturally fractured reservoirs. *Transport Porous Media* 83, 699–709.
- Li, Q., Jew, A.D., Kiss, A., Kohli, A., Maher, K., Brown Jr., G.E., Bargar, J.R., 2019a. Thicknesses of chemically altered zones in the shale matrices from interactions with hydraulic fracturing fluid. *Energy Fuels* 33 (8), 6878–6889.
- Li, Q., Jew, A.D., Cercone, D., Bargar, J.R., Brown, G.E., Maher, K., 2019b. Geochemical modeling of iron (hydr) oxide scale formation during hydraulic fracturing operations. In: *Unconventional Resources Technology Conference. Unconventional Resources Technology Conference (URTEC); Society of Exploration Geophysicists, Denver, Colorado*, pp. 22–24. July 2019 (pp. 3863–3876).
- Li, Q., Jew, A.D., Brown Jr., G.E., Bargar, J.R., Maher, K., 2020. Reactive transport modeling of shale-fluid interactions after imbibition of fracturing fluids. *Energy Fuels* 34 (5), 5511–5523.
- Ma, S., Morrow, N.R., Zhang, X., 1997. Generalized scaling of spontaneous imbibition data for strongly water-wet systems. *J. Petrol. Sci. Eng.* 18 (3–4), 165–178.
- Menefee, A.H., Welch, N.J., Frash, L.P., Hicks, W., Carey, J.W., Ellis, B.R., 2020. Rapid mineral precipitation during shear fracturing of carbonate-rich shales. *J. Geophys. Res. Solid Earth* 125, e2019JB018864.
- Newell, D.L., Carey, W., 2013. Experimental evaluation of wellbore integrity along the cement-rock boundary. *Environ. Sci. Technol.* 47 (1), 276–282.
- Noël, V., Spielman-Sun, E., Druhan, J.L., Fan, W., Jew, A.D., Kovscek, A.R., Brown Jr., G.E., Bargar, J.R., 2020. Synchrotron X-Ray Imaging of Element Transport Resulting from Unconventional Stimulation in Unconventional Resources Technology Conference URTEC-2020-3295-MS.
- Orem, W., Tatu, C., Varonka, M., Lerch, H., Bates, A., Engle, M., Crosby, L., McIntosh, J., 2014. Organic substances in produced and formation water from unconventional natural gas extraction in coal and shale. *Int. J. Coal Geol.* 126, 20e31.
- Qajar, J., Francois, N., Arns, C.H., 2013. Microtomographic characterization of dissolution-induced local porosity changes including fines migration in carbonate rock. *SPE J.* 18, 545–562, 03.
- Rangel-German, E.R., Kovscek, A.R., 2002. Experimental and analytical study of multidimensional imbibition in fractured porous media. *J. Petrol. Sci. Eng.* 36 (1–2), 45–60.
- Renock, D., Landis, J.D., Sharma, M., 2016. Reductive weathering of black shale and release of barium during hydraulic fracturing. *Appl. Geochem.* 65, 73e86.
- Rowan, E.L., Engle, M.A., Kraemer, T.F., Schroeder, K.T., Hammack, R.W., Doughten, M.W., 2015. Geochemical and isotopic evolution of water produced from Middle Devonian Marcellus shale gas wells, Appalachian basin, Pennsylvania. *Am. Assoc. Petrol. Geol. Bull.* 99, 181e206.
- Schindelin, J., Arganda-Carreras, I., Frise, E., Kaynig, V., Longair, M., Pietzsch, T., Preibisch, S., Rueden, C., Saalfeld, S., Schmid, B., Tinevez, J.-Y., White, D.J., Hartenstein, V., Eliceiri, K., Tomancak, P., Cardona, A., 2012. Fiji: an open-source platform for biological-image analysis. *Nat. Methods* 9 (7), 676.
- Shih, J.-S., Sakers, J.E., Anisfeld, S.C., Chu, Z., Muehlenbachs, L.A., Olmstead, S.M., 2015. Characterization and analysis of liquid waste from Marcellus shale gas development. *Environ. Sci. Technol.* 49, 9557e9565.
- Steefel, C.I., Appelo, C.A.J., Arora, B., Jacques, D., Kalbacher, T., Kolditz, O., Lagneau, V., Lichtner, P.C., Mayer, K.U., Meeussen, J.C.L., Molins, S., Moulton, D., Shao, H., Simunek, J., Spycher, N., Yabusaki, S.B., Yeh, G.T., 2015. Reactive transport codes for subsurface environmental simulation. *Comput. Geosci.* 19, 445–478.
- Stringfellow, W.T., Domen, J.K., Camarillo, M.K., Sandelin, W.L., Borglin, S., 2014. Physical, chemical, and biological characteristics of compounds used in hydraulic fracturing. *J. Hazard Mater.* 275, 37e54.
- Tokunaga, T.K., Wan, J., Jung, J.-W., Kim, T.W., Kim, Y., Dong, W., 2013. Capillary pressure and saturation relations for supercritical CO₂ and brine in sand: high-pressure P_c(S_w) controller/meter measurements and capillary scaling predictions. *Water Resour. Res.* 49, 4566–4579.
- Tokunaga, T.K., 2020. Simplified Green-Ampt model, imbibition-based estimates of permeability, and implications for leak-off in hydraulic fracturing. *Water Resour. Res.* 56 (4), e2019WR026919.
- Vankeuren, A.N.P., Hakala, J.A., Jarvis, K., Moore, J.E., 2017. Mineral reactions in shale gas reservoirs: barite scale formation from reusing produced water as hydraulic fracturing fluid. *Environ. Sci. Technol.* 51 (16), 9391–9402.
- Webb, S.M., 2011. The MicroAnalysis Toolkit: X-ray fluorescence image processing software. *Am. Inst. Phys. Conf. Proc.* 1365196–1365199.
- Wu, W., Sharma, M.M., 2017. Acid fracturing in shales: effect of dilute acid on properties and pore structure of shale. *SPE Prod. Oper.* 32, 051–063, 01.
- Zhou, X., Morrow, N., Ma, S., 2000. Interrelationship of wettability, initial water saturation, aging time, and oil recovery by spontaneous imbibition and waterflooding. *SPE J.* 5 (2), 21–24.
- Zhou, T., Zhang, S., Yang, L., Ma, X., Zou, Y., Lin, H., 2016. Experimental investigation on fracture surface strength softening induced by fracturing fluid imbibition and its impacts on flow conductivity in shale reservoirs. *J. Nat. Gas Sci. Eng.* 36, 893–905.
- Ziemkiewicz, P.F., He, Y.T., 2015. Evolution of water chemistry during Marcellus shale gas development: a case study in West Virginia. *Chemosphere* 134, 224e231.
- Zolfaghari, A., Dehghanpour, H., Noel, V., Bearinger, D., 2016. Laboratory and field analysis of flowback water from gas shales. *J. Unconv. Oil Gas. Resour.* 14, 113e127.